Supporting Information

Flux-Assisted Synthesis of a Visible-Light-Active La_2FeTiO_6 Double Perovskite with Intrinsic Bifunctional Activity for Photocatalytic Water Reduction and Oxidation

Bo Chen[a] ‡, Ahmed Mahmoud Idris[b] ‡, Ping Lu[a], Qiawen Shou[a], Khakemin Khan[c], Guocan Jiang[a]* and Zhengquan Li [a,d]**

[a] *School of Physics and Electronic Information Engineering,Zhejiang Institute of Photoelectronics, Zhejiang Normal University, Jinhua, Zhejiang 321004, China*

[b] *School of Electronic Information, Xijing University, Xi'an, 710123, China*

[c] *Department of Physics, University of Trento, Via Sommarive 14, 38123, Trento, Italy*

[d] *Key Laboratory of the Ministry of Education for Advanced Catalysis Materials, Zhejiang Normal University, Jinhua, Zhejiang 321004, China*

**Corresponding authors. E-mail addresses: ahmed63@163.com (A. M. Idris), gcjiang@zjnu.edu.cn (G. J), zqli@zjnu.edu.cn (Z. Li)*

Experimental Section

Chemicals and reagents

All of the chemicals and reagents used in this work were analytical grade and used as received without any purification. La_2O_3 (99.999%, Aladdin), Fe_2O_3 (99.0%, J&K Scientific), and TiO_2 (99.8%, Aladdin) were used as raw materials. NaCl (99.5%, Meryer) and KCl (99.5%, Meryer) were employed as the fluxing salt. $RuCl_3 \cdot xH_2O$ (99%, Aladdin) and $H_2PtCl_6 \cdot 6H_2O$ (AR, Aladdin) were used as precursors for the cocatalyst. $AgNO_3$ (AR, Sinopharm Chemical), $NaIO_3$ (99%, Aladdin), $Fe(NO_3)_3 \cdot 9H_2O$ (98.5%, Sinopharm Chemical), $Na_2S \cdot 9H_2O$ (98%, Aladdin), and Na_2SO_3 (AR, Sinopharm Chemical) were used as sacrificial reagents for electron-accepting and donating reagents, respectively. All the solutions were prepared using deionized water (18.2 MΩ) as a solvent.

Synthesis of La_2FeTiO_6

La_2FeTiO_6 (LFTO) double perovskite oxide was prepared by the flux method, wherein a stoichiometric 2:1:1 molar ratio of La_2O_3, Fe_2O_3, and TiO_2 precursors was mixed with NaCl/KCl (NaCl/KCl with a mass ratio of 1:1) molten salt. The mass ratio of LFTO to the molten salt was 1:4. The powder was thoroughly mixed for 1 h using an agate mortar, transferred into an alumina crucible, and then calcined at 900°C in a muffle furnace for 10 h. After naturally cooling down to room temperature, the obtained powder was washed with hot deionized water and ethanol several times to get rid of the fluxing salt. Finally, the sample was dried in a vacuum oven at 80°C overnight. For comparison, La_2FeTiO_6 powder was also synthesized by the traditional solid-state reaction method, denoted as LFTO-S. The raw materials were mixed according to the chemical ingredient ratio as mentioned above, without adding fluxing salts. The mixture was milled carefully for 1 h using an agate mortar, followed by calcination at 1150 °C for 24 h.

Deposition of Cocatalysts

Oxidation cocatalyst RuO_2 and reduction cocatalyst Pt were loaded by the in situ photodeposition method using $RuCl_3 \cdot xH_2O$ as a Ru precursor and $H_2PtCl_6 \cdot 6H_2O$ as a Pt precursor. Typically, 0.50 g of photocatalyst powder and calculated amounts of Ru precursors (1 wt%) or Pt precursors (0.5 wt%) were suspended in 100 mL of deionized water. Excess amounts of $NaIO_3$ or methanol were used as as sacrificial electron accepting or electron donating reagents for the oxidation deposition of RuO_2 or photoreduction deposition of Pt, respectively. The suspension was photoirradiated by a 300 W Xe-lamp ($\lambda \geq 420$ nm) under continuous stirring for 3 h, followed by filtration and washing with deionized water several times. Finally, the sample was dried in a vacuum oven at 80°C overnight.

Sample Characterizations

Scanning electron microscopy (SEM) and energy dispersive X-ray spectroscopy (EDX) were performed on a GeminiSEM 300 scanning electron microscope.

Transmission electron microscopy (TEM) and high-resolution TEM (HRTEM) analyses were performed using a JEOL JEM-2100F field-emission transmission electron microscope operating at 200 kV.

Powder X-ray diffraction (XRD) patterns were recorded by using a Philips X'Pert Pro Super X-ray diffractometer with Cu-Kα radiation (λ =1.5418Å).

The elemental contents of the samples were investigated by adopting X-ray fluorescence (XRF) (Shimadzu, XRF-1800).

UV-vis diffuse reflectance spectra were measured using a Hitachi U-4100 UV-Vis spectrophotometer equipped with an integration sphere for diffuse reflectance.

X-ray photoelectron spectra (XPS) were collected on an ESCALab 250 X-ray photoelectron spectrometer with Al-Kα radiation and carbon source (C 1s=284.8 eV) as the standard calibration binding energy.

Steady-state photoluminescence (PL) spectra were scanned on a spectrofluorometer (FluoroMax-4, Horiba Scientific).

Nitrogen adsorption experiments were performed with a Quantachrome NOVA 3000e system at 77 K. The sample was degassed at 373 K for ~72 h under vacuum before the

measurement. The filling rod was used to reduce the dead volume, thus improving the measurement accuracy. The specific surface area was calculated by using the multi-point BET equation ($0.1 < p/p_0 < 0.3$). The pore size distribution was derived by using the non-local density functional theory (NLDFT) method (N_2 at 77 K on carbon) based on a slit pore geometry. The total pore volume was calculated at $p/p_0 = 0.99$, similar to the value derived by the BJH (Barret–Joyner–Halender) method.

Electron paramagnetic resonance (EPR) was obtained using a Bruker EPR EMXplus spectrometer.

Photoelectrochemical measurement

The photoelectrochemical measurements were carried out using a three-electrode cell CHI 760E electrochemical station (Shanghai Chenhua, China) with a Pt foil counter electrode and a saturated Ag/AgCl reference electrode. The working electrode was prepared by the dip-coating method. 3 mg of catalyst was ultrasonically dispersed in 50 μL of absolute ethanol and 10 μL of 5 wt% Nafion solution, then deposited on FTO conductive glass with an exposed surface area of about 1 cm^{-2}. The three electrodes were inserted in a quartz cell filled with 0.5 M Na_2SO_4 electrolyte (electrolyte pH was buffered either with 1 M NaOH or 1M H_2SO_4). The variation of photoinduced current density versus time (I-t curve) was recorded at a 0 V bias potential under light switching on and off mode, $\lambda \geq 420$ nm, 300 W Xe lamp (SolarEdge 700). The electrochemical impedance spectroscopy (EIS) and Mott-Schottky (MS) results were obtained at the open circuit potential using a frequency range from 10^4 Hz to 10^{-1} Hz.

Photocatalytic Activity Measurement

Photocatalytic OER and HER activities were performed in an online photocatalytic analysis system (Labsolar-III AI, Beijing Perfectlight Technology Co., Ltd., China). The reaction was carried out in a top-irradiated reactor with an external cooling jacket, and a magnetic stirrer was placed at the bottom to provide stirring at 500 rpm. Typically, a 50 mg prepared photocatalyst was dispersed in the mixture of 100 mL deionized water and 0.02 M $AgNO_3$ ($NaIO_3$, $Fe(NO_3)_3$) or 0.1 M Na_2S+Na_2SO_3. After degassing under

vacuum to completely remove air, the reaction solution was irradiated by a 300 W Xe-lamp with a cut-off filter ($\lambda \geq 420$ nm). The irradiance was measured with a radiometer (FZ-A, Beijing Shida Photoelectric Technology Co., Ltd.), and the average irradiance was determined to be 100 mW/cm² by the five-point method. During the irradiation, the reaction temperature was maintained at 5°C by cycling water. The generated gases were analyzed by an online gas chromatography (GC-9790 II, Fuli, TCD), using Ar as the carrier.

Measurement of apparent quantum efficiency (AQE)

The apparent quantum efficiency (AQE) for the OER was estimated in terms of the following equation. In addition to different light sources, all the reaction conditions were the same as those of the above photocatalytic reaction. A 300 W Xe-lamp with a 420 nm band-pass filter was used as the light source.

$$AQE(\%) = \frac{4 \times moles\ of\ O_2}{Number\ of\ incident\ photons} \times 100\%$$

$$AQE(\%) = \frac{4 \times M \times A \times h \times c}{S \times P \times T \times \lambda} \times 100\%$$

Where A is the Avogadro constant (6.02×10^{23} mol^{-1}), h is Planck's constant (6.626×10^{-34} J s^{-1}), c is the speed of light (3×10^{8} m s^{-1}), S is the irradiation area (18.08 cm^2), P is the average light intensity (We used a standard five-point method, measuring at the center and four symmetric points around the periphery of the circular irradiation area, the average light intensity was calculated as 1.7 mW/cm^2), T is the photoreaction time (1 h = 3600 s), and λ is the wavelength of monochromatic light (420 nm), M is the number of moles of O_2 generated by RuO_2-LFTO in 1 h (4.2 μmol). The apparent quantum efficiency (AQE) of RuO_2-LFTO for the photocatalytic O_2 evolution reaction was finally calculated as 4.3% at 420 nm. For comparison, the AQE of RuO_2-LFTO-S for the photocatalytic O_2 evolution reaction was finally calculated as 1.9% under the same conditions.

DFT simulations

In this work, all first-principles calculations were performed based on spin-polarized density functional theory (DFT) as implemented in the Vienna Ab initio Simulation Package (VASP). The projector augmented-wave (PAW) method was employed to describe the interaction between ion cores and valence electrons. The Perdew-Burke-Ernzerhof (PBE) functional within the generalized gradient approximation (GGA) was used for the exchange-correlation term. A plane-wave kinetic energy cutoff of 520 eV was consistently applied for all calculations. The Brillouin zone was sampled using Γ-centered Monkhorst-Pack k-point meshes. For structural relaxations, a 6 × 6 × 6 k-point mesh was used. For the subsequent static self-consistent calculations to obtain accurate electronic properties, such as the density of states (DOS), a denser [9 × 9 × 9] k-point mesh was employed. Both the lattice parameters and the atomic positions were fully relaxed until the Hellmann-Feynman forces on each atom were less than 0.01 eV/Å, and the electronic self-consistency loop was converged to 1×10^{-6} eV. To account for the strong on-site Coulomb repulsion of the localized d-electrons of Ti and Fe, the DFT+U methodology was adopted in the simplified rotationally invariant approach proposed by Dudarev et al. Based on values commonly reported in the literature for similar oxide systems, the effective Hubbard parameters (U-eff = U-J) were set to 4.4 eV for the Ti 3d orbitals and 4.6 eV for the Fe 3d orbitals.

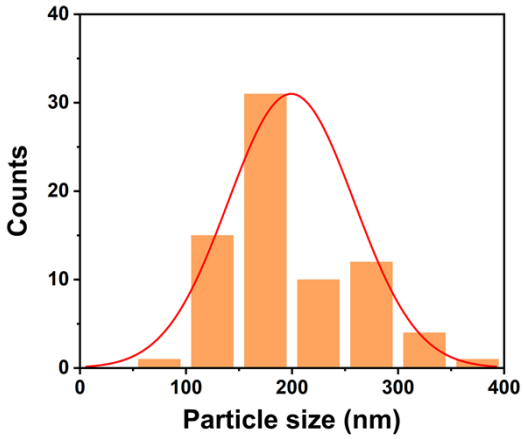

Figure S1. The histogram for the particle size distribution of LFTO derived from SEM images.

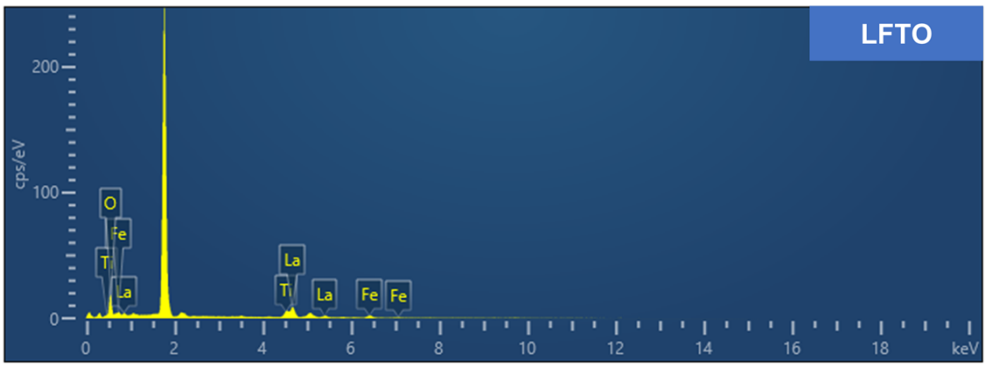

Figure S2. SEM elemental analysis of LFTO.

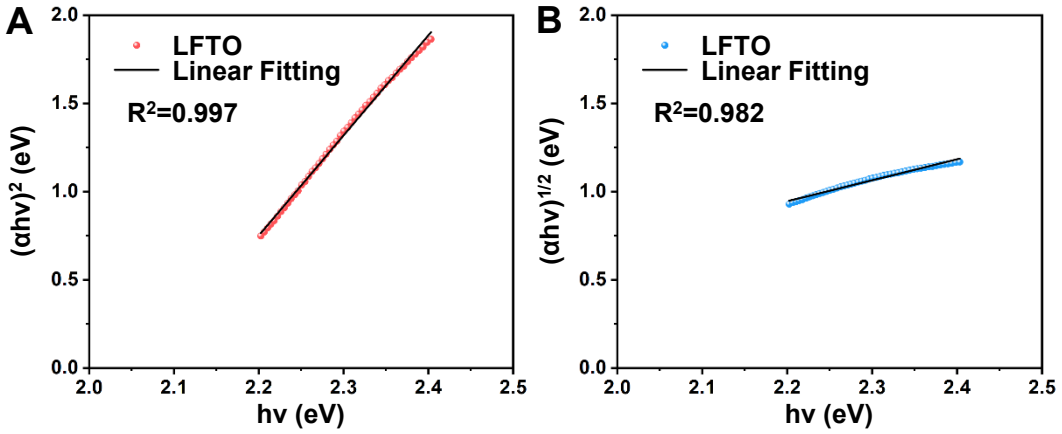

Figure S3. Tauc plots for optical band gap determination of LFTO. (A) Direct band gap plot of $(\alpha h\nu)^2$ vs. photon energy. (B) Indirect band gap plot of $(\alpha h\nu)^{1/2}$ vs. photon energy.

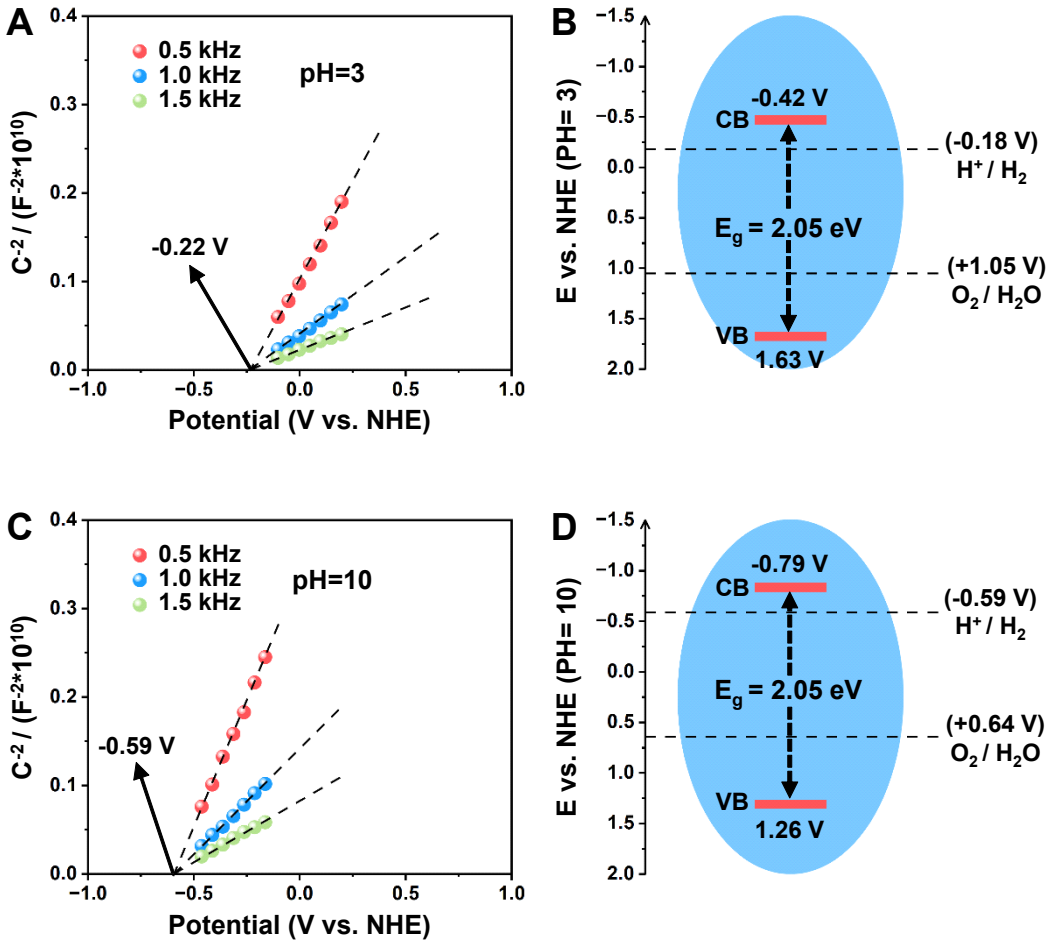

Figure S4. Mott-Schottky plots and a schematic diagram of the estimated band positions of LFTO in different pH levels. (A and B) pH=3. (C and D) pH=10.

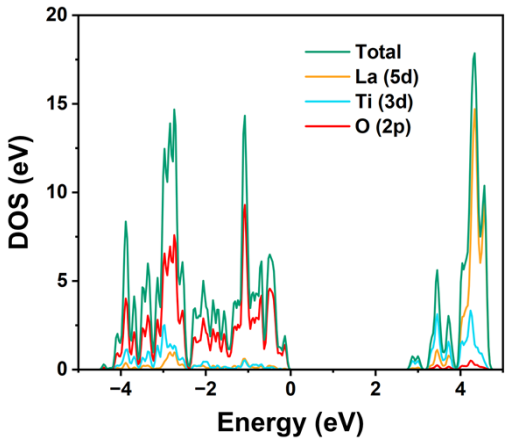

Figure S5. Density of States (DOS) of $LaTiO_3$.

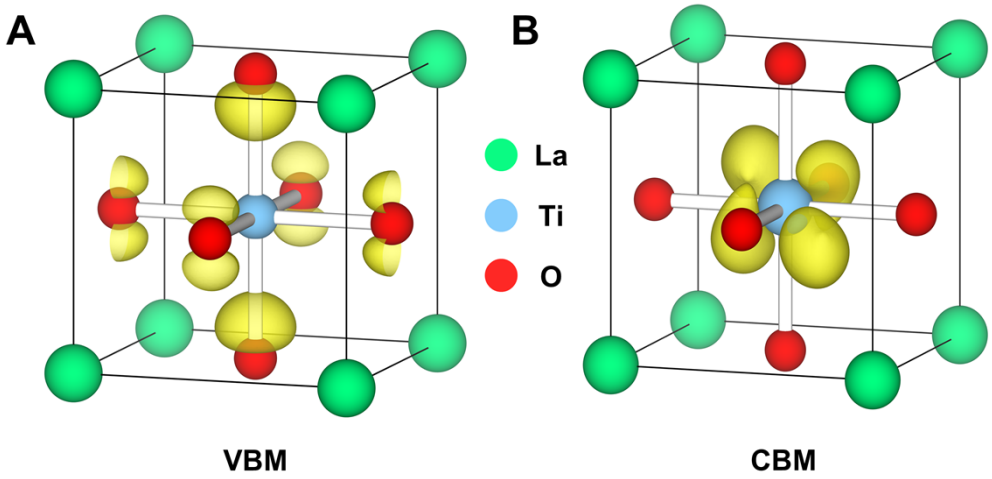

Figure S6. Charge distributions of (A) VBM and (B) CBM for $LaTiO_3$, respectively.

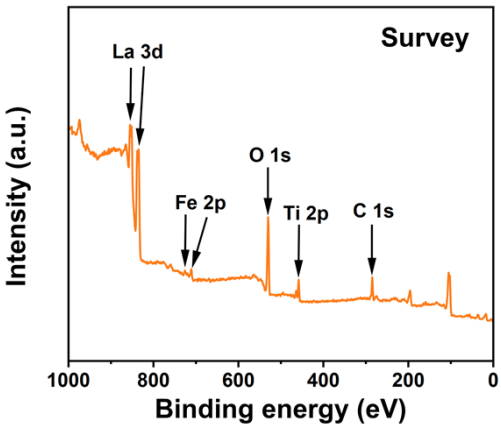

Figure S7. XPS survey of LFTO.

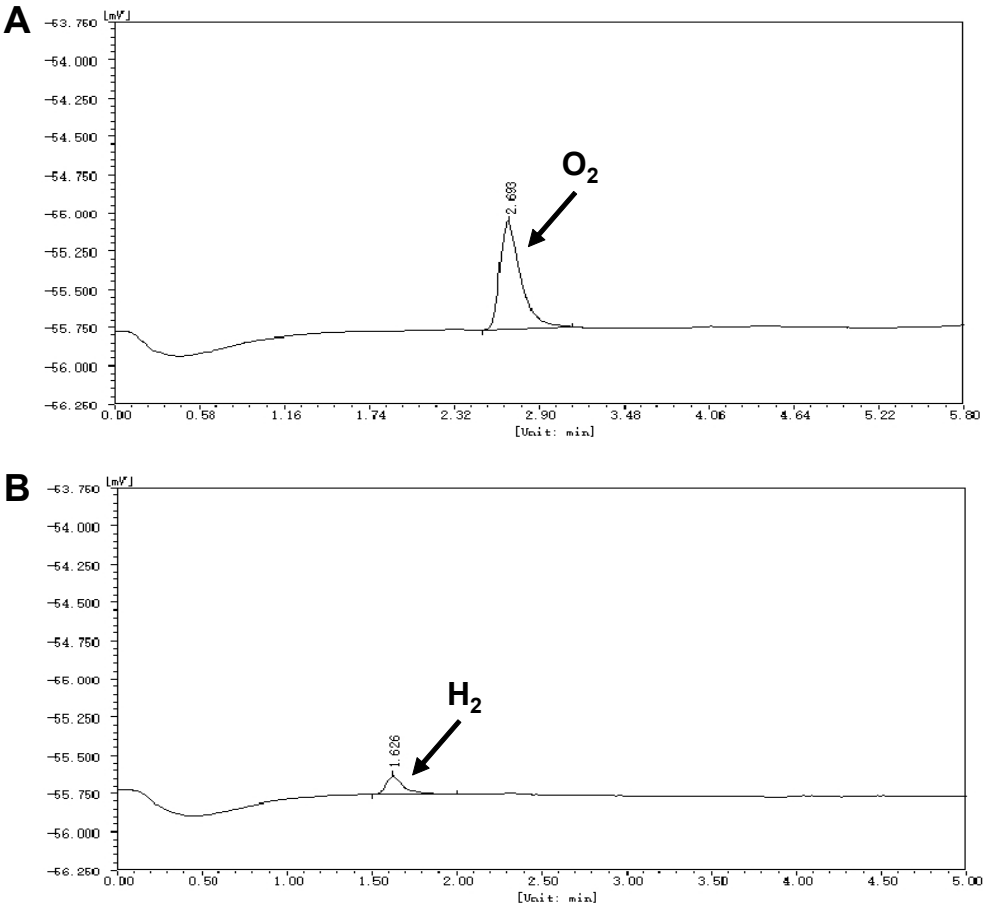

Figure S8. The original GC graph from the TCD detector for (A) H_2 and (B) O_2.

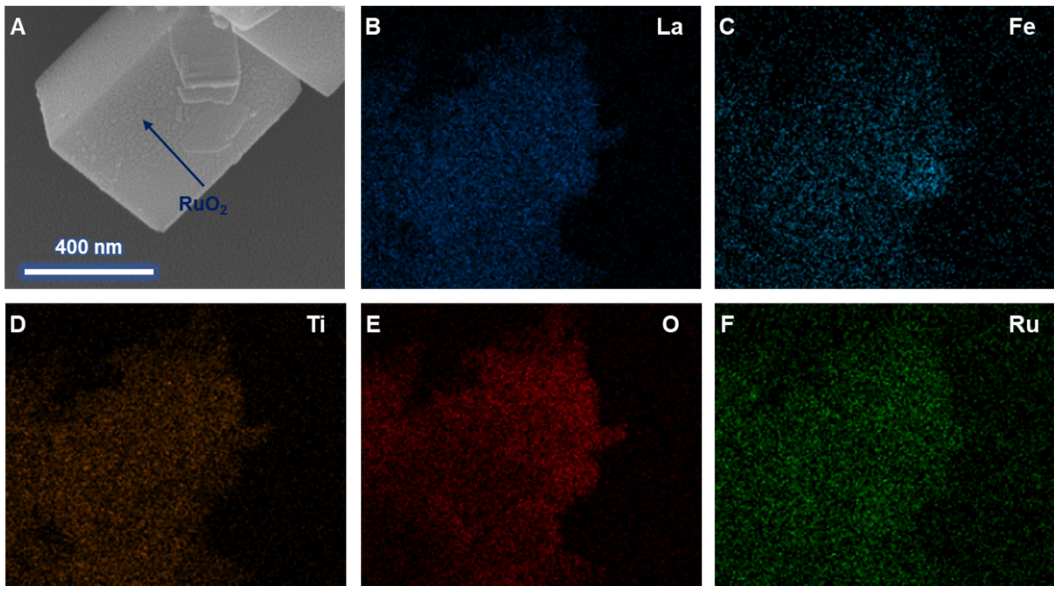

Figure S9. (A) SEM images of RuO_2-LFTO. (B−F) Elemental mapping of La, Fe, Ti, O and Ru, respectively.

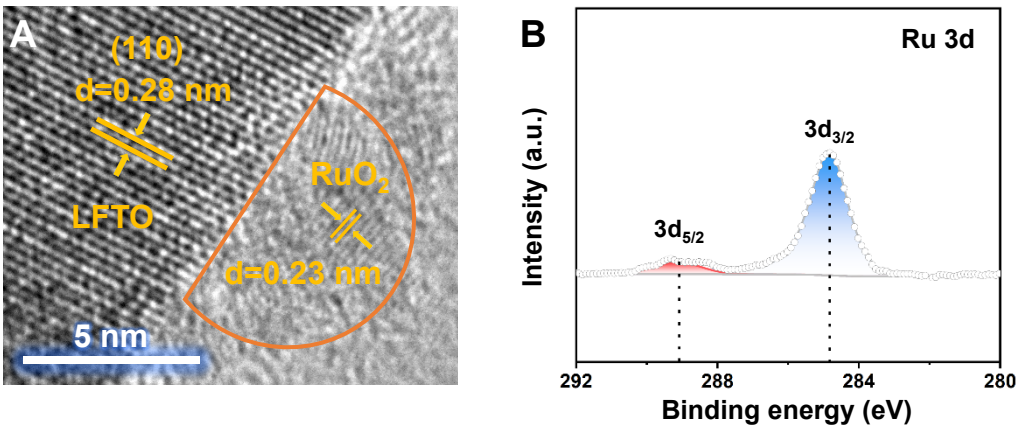

Figure S10. (A) HRTEM image of RuO_2-LFTO. (B) XPS analyses of Ru 3d.

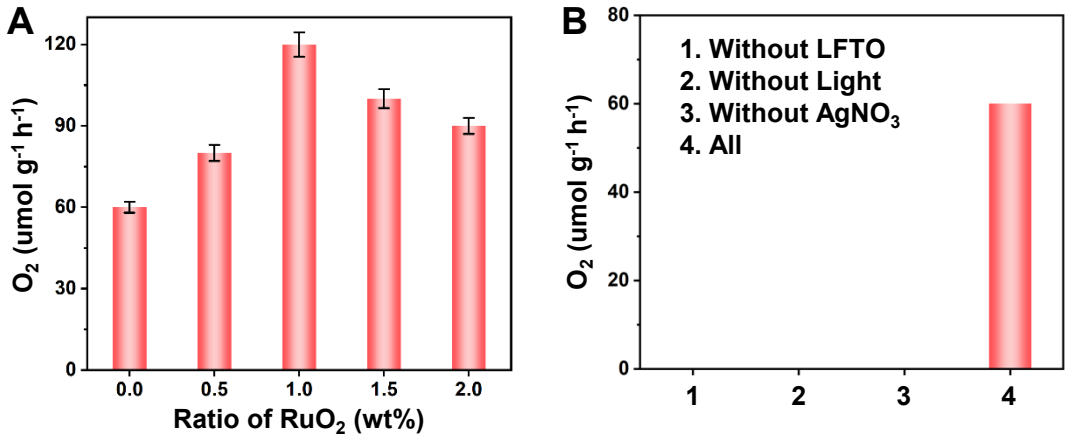

Figure S11. (A) Optimization of the loading amount of RuO_2. (B) Control photocatalytic experiments under different conditions for OER.

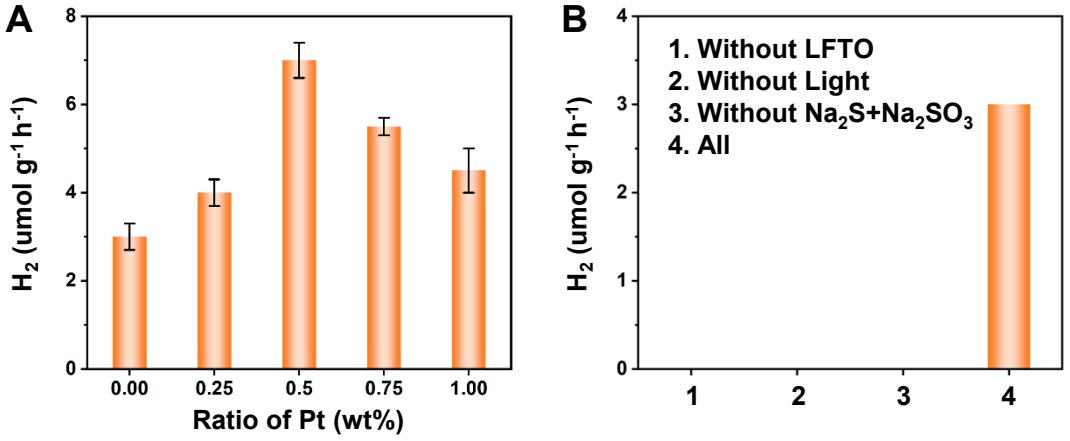

Figure S12. (A) Optimization of loading amount Pt. (B) Control photocatalytic experiments under different conditions for HER.

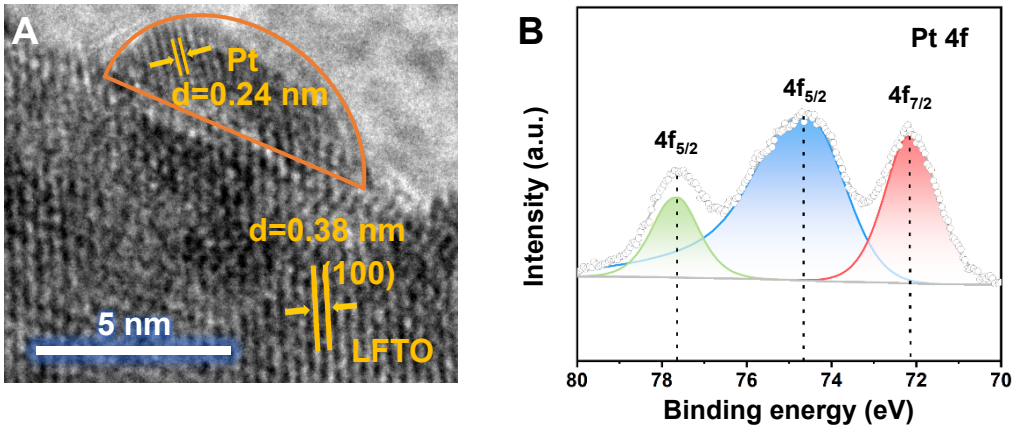

Figure S13. (A) HRTEM image of Pt-LFTO. (B) XPS analyses of Pt 4f.

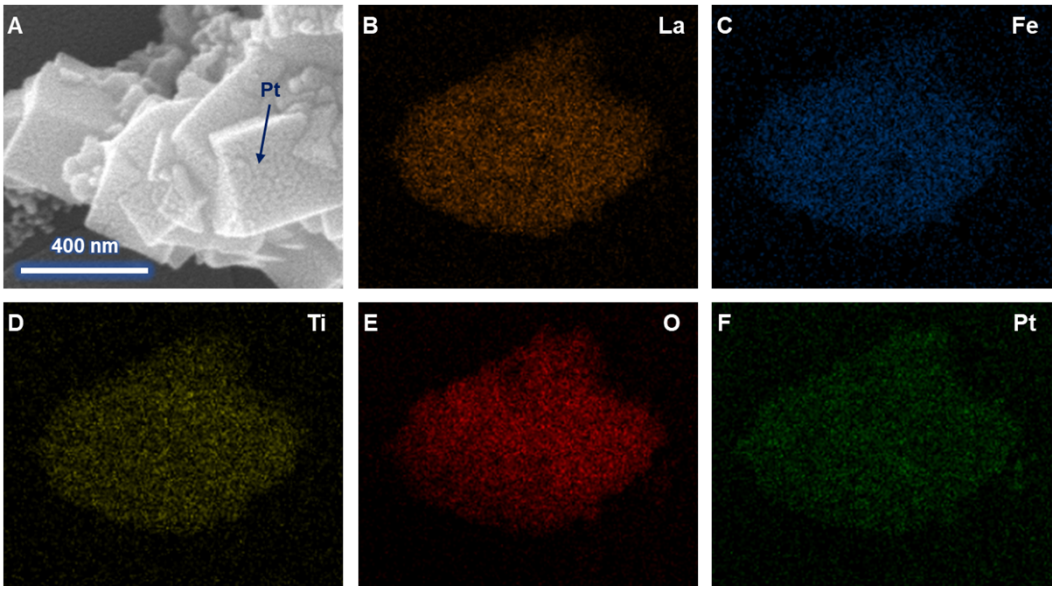

Figure S14. (A) SEM images of Pt-LFTO. (B−F) Elemental mapping of La, Fe, Ti, O and Pt, respectively.

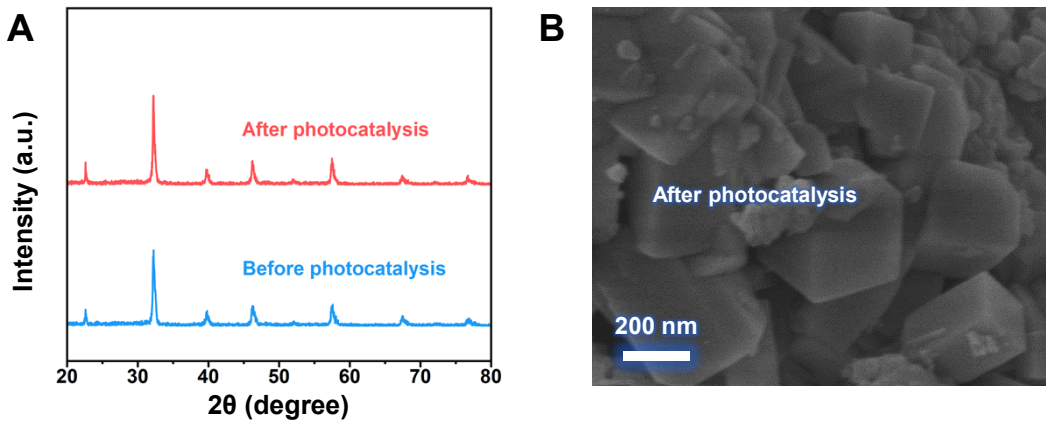

Figure S15. (A) XRD patterns of LFTO before and after photocatalysis. (B) SEM image of LFTO after photocatalysis.

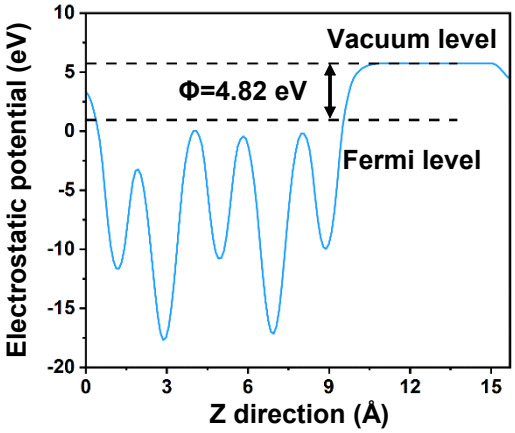

Figure S16. The calculated work function of LFTO.

Figure S17. Schematic illustration of Pt-LFTO and RuO_2-LFTO Schottky heterojunction formation, charge separation/transfer mechanism.

Figure S18. (A) XRD patterns of LFTO-S and LFTO. (B) SEM image of LFTO-S. (C) DRS spectra and Tauc plots of LFTO-S and LFTO. (D) EPR spectra of LFTO-S and LFTO.

The X-ray diffraction (XRD) patterns confirmed that phase purity in LFTO-S is achieved only after prolonged high-temperature calcination (1150 °C, 24 h) (Figure S18A). Consistently, the SEM image revealed that LFTO-S consists of irregularly aggregated particles ranging from several hundred nanometers to a few micrometers in size (Figure S18B). BET measurements showed a reduced specific surface area for LFTO-S (2.101 $m^2\ g^{-1}$) compared with the flux-synthesized sample (2.393 $m^2\ g^{-1}$). Although UV–vis absorption and Tauc analyses revealed no significant optical differences between the two samples (Figure S18C). EPR spectra indicated a higher concentration of defects in the SSR sample (Figure S18D).

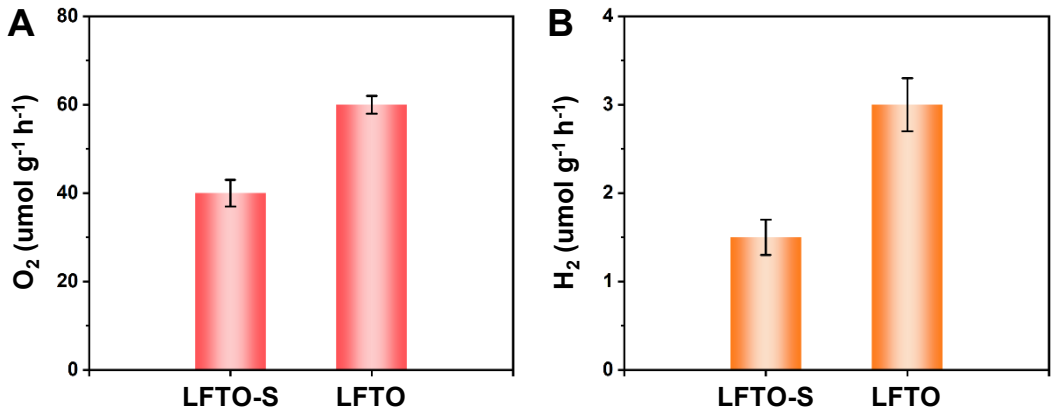

Figure S19. Compared the photocatalytic activities of LFTO-S and LFTO in (A) OER and (B) HER.

Table S1. Element composition of LFTO.

Element	Weight% (theoretical)	Weight% (XRF)	Atomic ratio
La	56.31	52.21	2
Fe	14.59	12.43	1
Ti	8.98	7.88	1
O	20.10	-	6

Table S2. Calculated electron and hole effective masses of different directions for LFTO.

Effective mass	Electron	Hole
m^* (101) / m_0	4.875	0.574
m^* (112) / m_0	1.339	0.586
m^* (111) / m_0	0.773	0.773
m^*_{ave} / m_0	2.329	0.644

Table S3. Calculated electron and hole effective masses of different directions for LTO.

Effective mass	Electron	Hole
m^* (110) / m_0	0.171	0.171
m^* (111) / m_0	0.191	0.191
m^*_{ave} / m_0	0.181	0.181

Table S4. Comparison of Photocatalytic Water Splitting activities on some oxide-based photocatalysts.

Photocatalysts	Bandgap (eV)	Sacrificial reagent	Cocatalysts	H_2 evolution (μmol g^{-1} h^{-1})	O_2 evolution (μmol g^{-1} h^{-1})	Reference
La_2FeTiO_6	2.05	Na_2S + Na_2SO_3	None	3	-	**This work**
			Pt	7	-	
		$AgNO_3$	None	-	60	
			RuO_2	-	120	
γ-Ga_2O_3	4.69	None	None	21.9	-	1
3Sr-Ga_2O_3/(Rh/Cr_2O_3)	4.44	None	Rh/Cr_2O_3	173.3	86.7	
Ca_2NiWO_6	2.8	$AgNO_3$	None	-	1.38	2
$Ca_2NiW_{0.97}Mo_{0.03}O_6$	2.18		None	-	2.65	
Sr_2CoTaO_6-F	2.7	Na_2S + Na_2SO_3	None	1	-	3
			Rh	4	-	
		$AgNO_3$	None	-	30	
			RuO_2	-	60	
Sr_2TiO_4-NF	2.57	None	$RhCrO_y$	30.25	15.25	4
Sr_2CuWO_6	2.07	Na_2SO_3	Pt	-	-	5
		$AgNO_3$	None	-	40	
			CoO_x	-	100	
Ba_2CuWO_6	2.21	Na_2SO_3	Pt	-	-	
		$AgNO_3$	None	-	-	
			CoO_x	-	60	
$PbTiO_3$	2.7	None	Rh/Cr_2O_3	32.9	17.4	6
Sr_2NiWO_6	2.88	$Na_2S_2O_8$	None	-	60	7
			RuO_2	-	116	
			Pt-RuO_2	-	420	
$LiCuTa_3O_9$	2.48	Na_2S + Na_2SO_3	None	-	-	8
			Rh_2O_3	0.55	-	
		$AgNO_3$	None	-	7.5	
			CoPi	-	95	
Bi_4TaO_8Br	2.53	MeOH	None	-	-	9
			Pt	0.125	-	
		AgNO3	None	-	90	
			RuO2	-	350	
Na-$La_2Ti_2O_7$	3.81	None	$Rh_{2-y}Cr_yO_3$	26.5	13	10

Reference

1 J. Shen, Y. Zhong, J. Lin, H. Li, C. Qiu, X. Liu, X. Wang, R. Hu, J. Long, X. Wang and Z. Zhang, *J. Catal.*, 2025, **443**, 115929.

2 Y. Luo, J. Xue, X. Zhu, J. Daniel, X. Gao, S. Sun, C. Gao and J. Bao, *RSC Adv.*, 2017, **7**, 5821-5826.

3 A. M. Idris, T. Liu, J. Hussain Shah, H. Han and C. Li, *ACS Sustain. Chem. Eng.*, 2020, **8**, 14190-14197.

4 J. Yu, J. Huang, R. Li, Y. Li, G. Liu and X. Xu, *Nat. Commun.*, 2025, **16**, 361.

5 E. Hua, S. Jin, S. Ni and X. Xu, *Inorg. Chem. Front.*, 2019, **6**, 2096-2103.

6 G. Wan, L. Yin, X. Chen, X. Xu, J. Huang, C. Zhen, H. Zhu, B. Huang, W. Hu, Z. Ren, H. Tian, L. Wang, G. Liu and H.-M. Cheng, *J. Am. Chem. Soc.*, 2022, **144**, 20342-20350.

7 A. M. Idris, T. Liu, J. Hussain Shah, A. S. Malik, D. Zhao, H. Han and C. Li, *ACS Appl. Mater. Interfaces*, 2020, **12**, 25938-25948.

8 B. Dong, J. Cui, T. Liu, Y. Gao, Y. Qi, D. Li, F. Xiong, F. Zhang and C. Li, *Adv. Energy Mater.*, 2018, **8**, 1801660.

9 X. Tao, Y. Zhao, L. Mu, S. Wang, R. Li and C. Li, *Adv. Energy Mater.*, 2018, **8**, 1701392.

10 L. Zhong, X. Li, Y. Zhan, Y. Liu, K. Yang, J. Liu, S. Liu, J. Jiang, L. Li and Y. Sakata, *Appl. Catal. A Gen.*, 2025, **692**, 120079.